Highlights

Global and direct solar irradiance estimation using deep learning and selected spectral satellite images

Shanlin Chen, Chengxi Li, Yuying Xie, Mengying Li

- 5-min GHI and DNI are estimated by deep learning and multispectral satellite images.
- Correlation analysis and attention mechanism are applied to improve the performance.
- Both GHI and DNI estimations are more accurate than the benchmark physical model.
- The proposed model shows substantial improvements in extracting cloud information.

Global and direct solar irradiance estimation using deep learning and selected spectral satellite images

Shanlin Chen[a], Chengxi Li[b], Yuying Xie[a], Mengying Li[a,c,*]

[a]*Department of Mechanical Engineering, The Hong Kong Polytechnic University, Hong Kong SAR*
[b]*Department of Industrial and Systems Engineering, The Hong Kong Polytechnic University, Hong Kong SAR*
[c]*Research Institute for Smart Energy, The Hong Kong Polytechnic University, Hong Kong SAR*

Abstract

To fully exploit the spectral information of modern geostationary satellites, this work proposes a deep learning model based on convolutional neural network and attention mechanism for 5-min ground-level global horizontal irradiance (GHI) and direct normal irradiance (DNI) estimations. Correlation analysis is performed to select the representative satellite bands, which can improve the modeling efficiency without accuracy loss when compared with the usage of all spectral bands. The results show that the proposed model produces GHI estimation with a normalized root mean squared error (nRMSE) of 20.57% and a normalized mean bias error (nMBE) of -2.04%, and the DNI estimation has an nRMSE of 23.63% and the nMBE is 0.36%. Compared with the national solar radiation database (NSRDB), the proposed model produces a GHI estimation with the nRMSE reduction of 5.15%. As for DNI estimation, the proposed method shows an nRMSE reduction of 13.77%. Meanwhile, the proposed models generally yield better GHI and DNI estimations under different intervals of clear-sky index than NSRDB. The combination of deep learning and remote sensing shows potential in better extracting the cloud information via multispectral satellite images, which can better support solar resourcing and forecasting applications, especially for cloudy conditions.

Keywords: Solar resource assessment, remote sensing, spectral satellite data, deep learning, correlation analysis

1. Introduction

Climate change, carbon neutrality and net zero emissions have drawn unprecedented attention worldwide among the energy-related industry and academia over the past decade [1]. Many countries have introduced their national energy policies and plans to reach the global climate goals [2]. Under such a blueprint, the rapid expansion and integration of renewable energy sources into current power systems in a near future could be foreseen [1]. It is predicted that the global electricity capacity of renewables will rise more than 60% between 2020 and 2026 [3]. Solar energy, as a promising candidate with worldwide potential, is set to be one of the primary power sources to enable the deep decarbonization in the energy sector. Despite the variability and intermittency, both solar photovoltaic (PV) and concentrated solar power (CSP) are important components on the pathway towards net zero emissions [4, 5]. The power production of solar PV or CSP is heavily related to the available solar irradiance, i.e., global horizontal irradiance (GHI) and direct normal irradiance (DNI), at the location of interest [6]. That said, as

*Corresponding author
Email address: mengying.li@polyu.edu.hk (Mengying Li)

long as solar energy is involved in the roadmap to carbon neutrality, the need for solar resource assessment and forecasting is essential in supporting solar energy projects [2, 7].

The uncertainty and intermittency of local irradiance leads to high variability in the power output of solar energy projects, which also introduces challenges in the system operation [8–10]. Solar resource assessment aims to support the feasibility study and optimal design of solar energy projects by projecting power demand and supply potentials, analyzing techno-economic viability and minimizing the long-term risks [2, 6, 11]. Ground irradiance measurements with careful calibrations are the most accurate data source in solar resource assessment. However, complete and long-term on-site measurements are not available at most locations due to associated technical and financial issues [12, 13]. Even though ground irradiance measurements are invaluable, their limited data availability greatly hinders the wider application [14]. On the other hand, the irradiance estimation and retrievals via remote sensing provide an alternative in the evaluation and design of solar energy projects [12, 15].

Satellite-to-irradiance algorithms can be broadly grouped as physical methods that based on radiative transfer and statistical methods [11, 16]. The physical solar model used in the National Solar Radiation Database (NSRDB) [17] and Heliosat-4 method [18] are the representatives of physical models, where the detailed interactions between solar radiation and atmospheric compositions are simulated using radiative transfer models (RTMs). The essential atmospheric inputs such as cloud properties, aerosol optical depth (AOD), and water vapor content can be obtained from geostationary satellites [17, 18], for instance, Geostationary Operational Environmental Satellite (GOES) and Meteosat Second Generation (MSG) satellites. Of statistical models, the pure empirical methods are of limited applications due to the inferior performance and lack of generality [11]; Semi-empirical methods rely on separate attenuation processes of cloud and other constituents in the atmosphere. Physical models are generally have better performance with more complexity, while semi-empirical models are easier to implement with a compromised performance. Both physical and semi-empirical methods show large uncertainties in estimating solar irradiance under cloudy conditions [19].

As the ground-truth in validating solar irradiance models, on-site measurements are of great importance [20]. Moreover, the local qualified observations in just a short period could be used in the processes to get long-term modeled data, for instance, site adaptation [21], and machine learning based models [22–24]. Given the high temporal and spatial information provided by the new generation satellites and the advancements in machine learning algorithms, the combination of machine learning (especially deep learning) and remote sensing, as an optimized statistical method, brings new insights in reducing the uncertainties of solar irradiance modeling [15, 25–27]. Lu et al. [28] applied all the bands of Multi-functional Transport Satellite (MTSAT) for daily GHI estimation with the aim to fully exploit the information of visible and infared channels. Jiang et al. [25] proposed a deep learning algorithm based on convolutional neural network (CNN) and multilayer perception (MLP) for hourly GHI estimation using images from visible channel of MTSAT, in an attempt to reduce the spatial effects related to the approximation of an independent pixel. Verma and Patil [29] presented a machine learning method for solar radiation assessment using pixels of multispectral Meteosat satellite images for the target location. Similarly, the iterative random forest model was adopted for estimating half-hourly global, direct, and diffuse components of solar irradiance using GOES-16 data and some viewing geometrical parameters [30, 31]. Rocha and Santos [32] reported a deep learning network based on CNN and long short-term memory (LSTM) network for GHI and DNI estimation using GOES-16 imagery of all channels. However, the developed model could not produce better GHI

estimation than NSRDB, while the improvement of DNI estimation remains limited.

To further exploit the application of new-generation geostationary satellite with much finer spatiotemporal resolution (i.e., 2-km and 5-min) in solar resource assessment, this work proposes a deep learning model with attention layer for high-resolution (5-min) GHI and DNI estimations. It is expected that the data with high spatiotemporal resolution and high accuracy can provide better resource information for designing solar energy projects, as it better captures the variability of solar irradiance [33]. Instead of using all spectral satellite bands, a correlation analysis is performed to select representative bands, which can improve the modeling efficiency and thus be beneficial for large-scale applications. To address the spatial effects such as nonlocal cloud shadows, multispectral images are applied as the input rather than single pixels. The major contributions of this work are summarized as follows:

- A correlation analysis is applied to select the representative satellite spectral bands, which can reduce the modeling complexity for satellite-to-irradiance mapping. This method is also beneficial for large-scale applications that involve long time periods and/or large areas of interest.
- The application of attention mechanism [34] and spectral satellite images around the target location aims to better account for the nonlocal cloud effect, which can improve the accuracy of irradiance estimations by deep learning.
- The estimates of 5-min GHI and DNI are benchmarked with NSRDB and show improved overall accuracy. Considering that NSRDB represents the state-of-the-art in satellite-to-irradiance methods, the improvements in irradiance estimations might bring more benefits to the solar community.
- Further evaluations and error analysis of irradiance estimations are performed to identify the sources of error and potential ways for future improvements.

The remainder of this paper is structured as follows: Section 2 describes the data and the methods for solar irradiance estimations. The performance of the proposed model for solar irradiance estimation and the comparisons with other models are presented in Section 3. Section 4 details the explanation and implication of the results. Finally, key findings are summarized in Section 5.

2. Data and methods

This section describes the used data and the deep learning method for estimating ground-level solar irradiance (i.e., GHI or DNI). As shown in the flowchart (see Fig. 1), the GOES-16 data of all bands are extracted from publicly available source. Then the cropped images for a location centered in the region of 11×11 pixels are pre-processed to be consistent in temporal and spatial resolutions. Images of selected bands from the correlation analysis are the inputs of the deep learning model, while the labels are clear-sky indexes obtained from irradiance measurements and Ineichen-Perez clear-sky model [35, 36]. The trained model is applied for estimating clear-sky index via new input data of GOES-16, and the solar irradiance estimation is obtained using the estimated clear-sky index and Ineichen-Perez clear-sky irradiance. Note that the methodologies for estimating GHI and DNI are the same, but deep learning models should be developed separately. The detailed descriptions of the used data and method are presented in the following subsections.

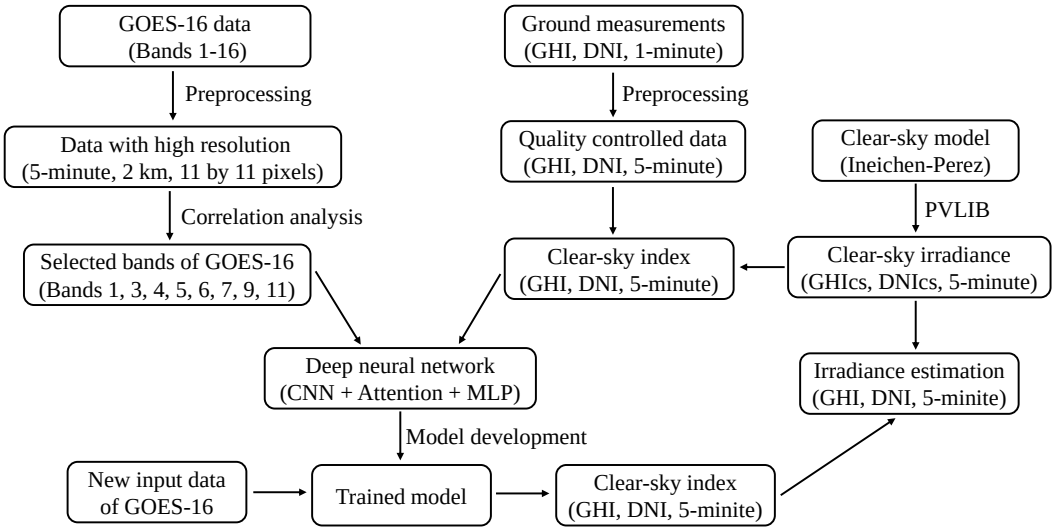

Figure 1: The flowchart of ground-level solar irradiance estimation using deep learning and satellite measurements of GOES-16.

2.1. Data

The data used in this work mainly includes spectral satellite images of GOES-16 and ground-level irradiance measurements from the Surface Radiation Budget Network (SURFRAD) stations [37]. GOES-16 (75.2° West), as one of the GOES-R series, is operated by National Oceanic and Atmospheric Association (NOAA). The Advanced Baseline Imager (ABI) has 16 spectral bands, which provide data with much finer temporal and spatial resolutions compared to the previous generations. The detailed information of each spectral band is presented in Table 1. 5-min spectral satellite measurements of all the 16 spectral bands in the year of 2019 are downloaded, which are then extracted as images and georeferenced to the target ground locations. The spectral satellite images are in the size of 11×11 pixels, and the target ground station locates at the center. Note that the spectral bands have different spatial resolutions as shown in Table 1. The spatial resolution is in the range of 0.5 - 2-km at the sub-satellite point, and spectral bands with better resolutions are therefore re-scaled to 2-km. The end timestamp of each scan in Coordinated Universal Time (UTC) is used to index the images after rounded to the next nearest 5-min interval. This is for the compatibility with ground irradiance measurements and real-time applications. Sample spectral images for one of the target locations are presented in Fig. 2, where the images have a size of 11×11 pixels and a spatial resolution of 2-km.

The ground-level irradiance measurements are from SURFRAD stations, namely, Bondville (BON), Desert Rock (DRA), Fort Peck (FPK), Goodwin Creek (GWN), Pennsylvania State University (PSU), Sioux Falls (SXF), and Table Mountain (TBL) as summarized in Table 2. Measurements including GHI, DNI, diffuse horizontal irradiance (DHI), solar zenith angle in 2019 at all the seven stations are obtained after quality control. Note that DHI is not of interest in this work, however, it is required in the classification of cloudy and clear periods [38] for the performance evaluation. All the measurements are in the 1-min temporal resolution and indexed in UTC time.

Due to the high airmass effect, all the irradiance measurements over the solar zenith angle of 85° are eliminated. Note that the satellite images are in the time resolution of 5-min, GHI and DNI are therefore aggregated into the same temporal resolution.

Table 1: The detailed information of the ABI spectral bands of GOES-16.

Band	λ [μm]	Center λ [μm]	Resolution [km]	Nickname	Type
1	0.45-0.49	0.47	1	Blue	Visible
2	0.59-0.69	0.64	0.5	Red	Visible
3	0.846-0.885	0.865	1	Veggie	Near-Infrared
4	1.371-1.386	1.378	2	Cirrus	Near-Infrared
5	1.58-1.64	1.61	1	Snow/Ice	Near-Infrared
6	2.225-2.275	2.25	2	Cloud particle size	Near-Infrared
7	3.80-4.00	3.90	2	Shortwave window	Infrared
8	5.77-6.60	6.19	2	Upper-level water vapor	Infrared
9	6.75-7.15	6.95	2	Mid-level water vapor	Infrared
10	7.24-7.44	7.34	2	Lower-level water vapor	Infrared
11	8.30-8.70	8.50	2	Cloud-top phase	Infrared
12	9.42-9.80	9.61	2	Ozone	Infrared
13	10.10-10.60	10.35	2	”Clean” longwave window	Infrared
14	10.80-11.60	11.20	2	Longwave window	Infrared
15	11.80-12.80	12.30	2	”Dirty” longwave window	Infrared
16	13.00-13.30	1.378	2	CO_2 longwave	Infrared

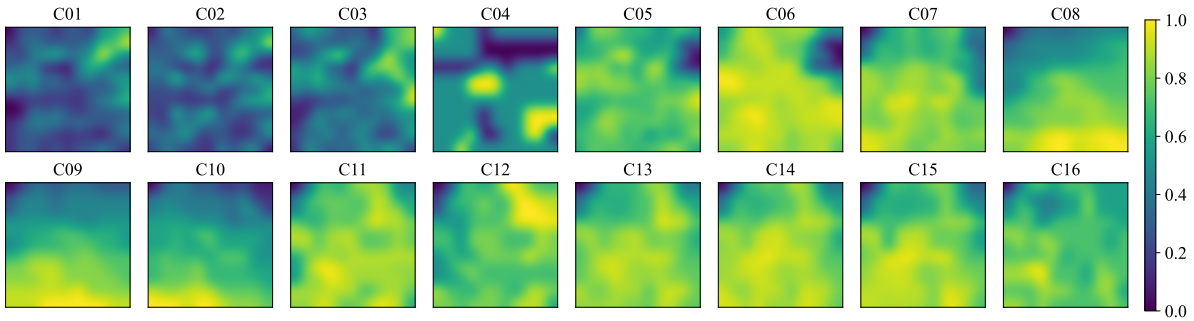

Figure 2: Sample satellite images including all the spectral bands of GOES-16 for Bondville (40.05°, -88.37°) at 2019-01-10 20:45:00 (UTC). The image is in the size of 11×11 pixels, where Bondville is located at the center. All the spectral images are normalized to the range of [0,1] using the Min-Max normalization.

Table 2: Detailed information of the seven SURFRAD stations. The climate is based on Köppen classifications. The elevation angle and azimuth angle are from the station to GOES-16, and the azimuth angle starts from the North (0°).

Station	Latitude (°)	Longitude (°)	Altitude (m)	Climate*	Elevation (°)	Azimuth (°)
BON	40.05	-88.37	230	Dfa	41.7	160.0
DRA	36.62	-116.02	1007	Bwk	29.9	124.6
FPK	48.31	-105.10	634	Bsk	47.2	155.0
GWN	34.25	-89.87	98	Cfa	27.5	142.4
PSU	40.72	-77.93	376	Dfb	42.8	175.8
SXF	43.73	-96.62	473	Dfa	35.2	150.4
TBL	40.12	-105.24	1689	Bsk	34.3	138.1

* Köppen climate classifications are: Bsk (arid, steppe, cold), Bwk (arid, desert, cold), Cfa (temperate, without dry season, hot summer), Dfa (continental, without dry season, hot summer), Dfb (continental, without dry season, warm summer).

The satellite-derived GHI and DNI provided by NSRDB [39] are used for comparison to evaluate the performance of the applied deep learning algorithms. Both GHI and DNI estimations of NSRDB for all the SURFRAD stations in 2019 are downloaded, with the spatiotemporal resolution of 2-km and 5-min. As a publicly available data source that is extensively accessed for solar energy applications, NSRDB is based on the physical solar model and the reanalysis products from many other associations [17]. Broadband irradiance including GHI, DNI, and other auxiliary variables such as cloud type, are available in NSRDB. Since 2018, the spatiotemporal resolution of NSRDB has been improved to 2-km and 5-min. Meanwhile, NSRDB represents the state-of-the-art in the satellite-based estimation of solar irradiance. Considering that other deep learning satellite-to-irradiance models usually have different locations of interest and various spatiotemporal resolutions, NSRDB is selected as the benchmark and its accuracy is validated against ground measurements [33].

2.2. Correlation analysis

In machine learning applications, feature selection is extensively applied to decrease the dimensionality by eliminating redundant and irrelevant features [40]. Feature selection has been proved to be helpful in understanding data, reducing the complexity, and improving the learning efficiency as well as predictive performance of machine learning tasks [40, 41]. Typically, feature selection methods can be grouped as filter and wrapper methods [40]. A filter method usually assesses the general characteristics of the dataset before the application of any machine learning algorithms. While a wrapper method requires a predefined learning algorithm in the process of feature selection, the features are selected based on the performance of the predetermined algorithm. Therefore, the wrapper method is more computationally expensive than the filter method [41].

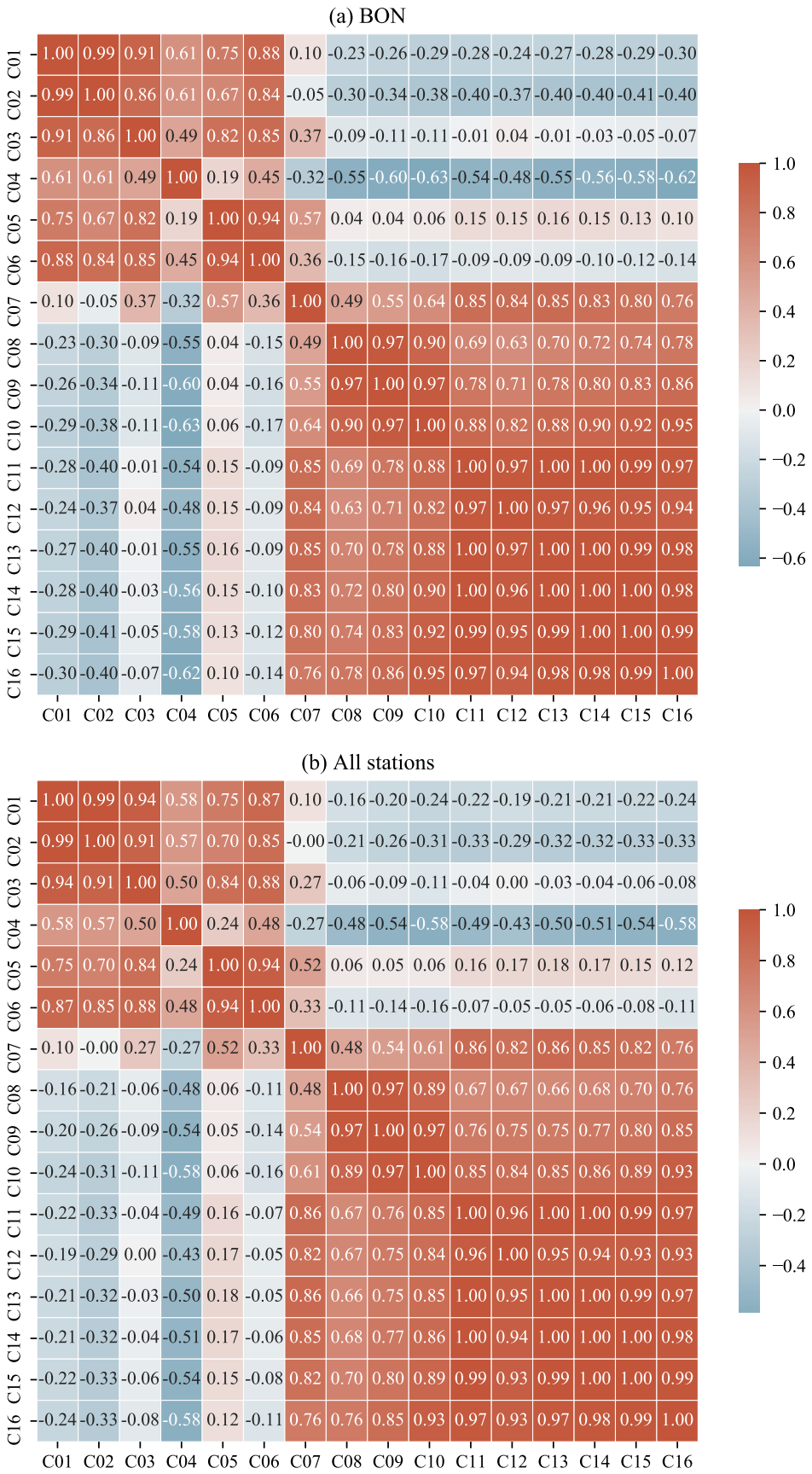

Figure 3: Correlation coefficients between measured radiance data of the 16 spectral bands of GOES-16 at (a) BON and (b) All SURFRAD stations.

In general, a good feature is relevant to the target but is not redundant to any other input features [42]. Feature correlation is usually applied to describe the similarity and redundancy among the features [42, 43]. A feature is defined to be redundant if it is highly correlated with one or more other features [42]. Therefore, a correlation analysis is performed among the measurements of 16 spectral bands of GOES-16 to reduce the input size. This can improve the modeling efficiency, especially for large-regional applications.

One commonly used measure of similarity between two variables (X, Y) is the correlation coefficient $r(X, Y)$, which is defined as

$$r(X, Y) = \frac{\sum(x_i - \overline{x})(y_i - \overline{y})}{\sqrt{\sum(x_i - \overline{x})^2}\sqrt{\sum(y_i - \overline{y})^2}} \quad (1)$$

where (x_i, y_i) are the paired data of (X,Y), $\overline{x}$ and $\overline{y}$ are the means of X and Y, respectively. The value of $r(X, Y)$ is inclusively between -1 and 1, with the value of 1 or -1 indicating X and Y are totally correlated. When X and Y are completely independent, the value of $r(X, Y)$ is 0.

The correlation analysis result for 16 spectral bands of GOES-16 is shown in Fig. 3. Fig. 3(a) presents the correlation coefficients of the 16 spectral bands at BON. There are some bands highly correlated, for instance, the coefficient of C12 and C13 is 1.00. Correlation analysis of GOES-16 bands at other SURFRAD stations have similar results, the overall coefficients involving all SURFRAD stations are shown in Fig. 3(b). Note that the correlation analysis is based on the satellite measurements at the target location with the pixel size of 1x1. When using more pixels, for example, 3x3 or 5x5, there are limited differences using averaged satellite measurements. It is shown in Fig. 3 that $r(X, Y) = r(Y, X)$ and $r(X, X) = 1.00$. A threshold of 0.95 is predefined to select the representative bands. In specific, if the coefficient of two channels is greater than 0.95, one of them is selected to represent the other. It is necessary to mention the selection of representative band for C08, C09, and C10. Since r(C08,C09) and r(C09,C10) are above the threshold, while r(C08,C10) is below it, C09 is selected to represent both C08 and C10. As a result, the selected bands are C01, C03, C04, C05, C06, C07, C09, and C11.

2.3. Deep learning model

With the improvement of computational ability and the advancement of learning algorithms, deep learning has attracted increasing attention in solar resource assessment and forecasting in the past decade [25, 44]. Deep learning introduces simper but more efficient representations that provide capabilities to build complex concepts in representation learning. Meanwhile, the depth of deep neural network (DNN) enables the multistep sequential instructions, which offer great power and flexibility in modeling complicated problems [45]. Different DNN structures have been proposed for solar irradiance modeling referring satellite and sky images [25, 46, 47].

The deep learning model proposed in this study employs convolutional, attention, and four fully connected dense layers as shown in Fig. 4. In specific, CNNs provide specialized neural networks to deal with data with a grid-structured topology such as images. Compared with fully connected networks, CNNs are more computationally efficient and easier in implementation and hyperparameters tuning [45]. As feed-forward neural networks, CNNs are powerful in extracting properties of input images, which can capture the features efficiently and reduce the amount of parameters. Convolutional layer is the core block of CNNs to discover local relationships via sparse connectivity, parameter sharing and equivariant representations [45]. An activation function (e.g., ReLU) is usually applied on the linear convolution results to introduce non-linearity on the output feature maps. While the pooling layer is to extract representative characteristics over local regions and reduce the dimension gradually

[45]. The attention layer is based on attention mechanism [34] that has been extensively adopted in different applications such as image analysis including satellite images [48]. The attention mechanism can process preceptual information efficiently and accurately, by focusing on the target area and suppressing other useless content [49]. Similarly, the attention mechanism in deep learning is to enable the model focus on the features that are more important to the current output [44], which can improve the performance of the model. While the dense layers are employed to learn the representations between the extracted input features and the targets.

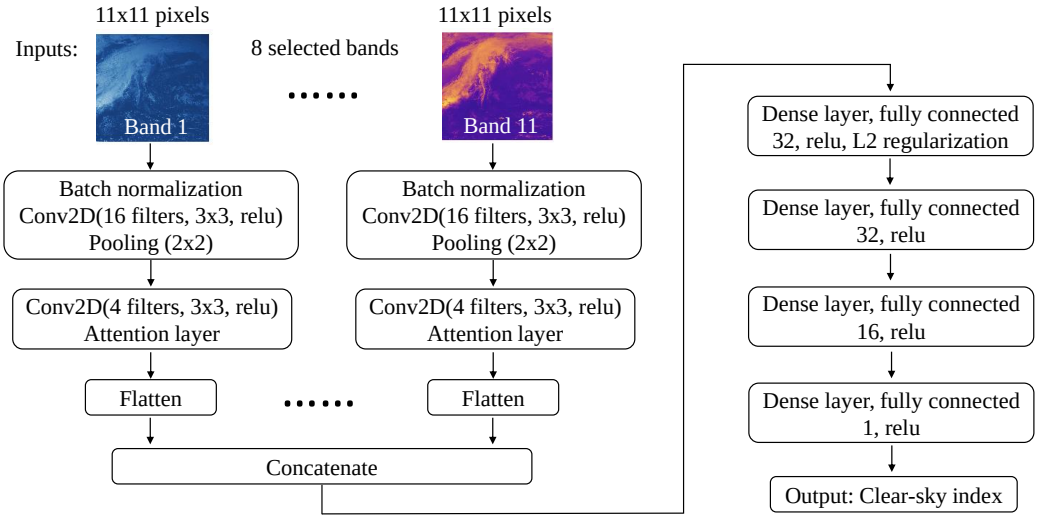

Figure 4: The structure of deep learning model for estimating ground solar irradiance using the GOES-16 images of selected bands. The inputs are images of 8 selected bands with size of 11×11 pixels, the output is the clear-sky index. Note that the hyperparameters might vary for different locations, this figure is just to show the structure.

The cropped satellite images of 8 selected GOES-16 bands are the inputs for the deep learning model based on Tensorflow [50]. As shown in Fig. 4, 8 images are processed parallelly via normalization, convolutional and attention layers. The extracted features of each image are then flattened and concatenated as the input vector of the four fully connected dense layers. The ReLU activation is applied in convolutional and dense layers, and the L2 regularization is to avoid over-fitting and improve the performance. The output is the clear-sky index, which is defined as the ratio between measured GHI and clear-sky GHI estimate. Clear-sky index is used to normalize the irradiance time series and reduce the seasonal and diurnal variations. Note that the clear-sky index is defined based on GHI. However, when developing the deep learning model for DNI estimation, the concept of clear-sky index is also adopted for DNI measurements and clear-sky DNI. Clear-sky GHI and clear-sky DNI are estimated by the Ineichen-Perez model [35] due to the simplicity. Although the Ineichen-Perez model has compromised performance in estimating clear-sky irradiance [51, 52], the impact on the final irradiance estimation remains limited as the estimated clear-sky index is converted back to irradiance components (i.e., GHI and DNI) by multiplying the clear-sky irradiance [53].

To better represent the yearly variations, data in March, June, September, and December are used for testing,

while the data in the remaining months in 2019 are used as training and validation sets (in which 20% of the data is used for validation). Adam is the applied optimizer and the Huber loss function is used to update the network parameters. The numbers of layers and units, the numbers of filters and kernel size, and other hyperparameters such as learning rate and regularization factor are optimally selected by grid search. In training the deep learning model, the Xavier initialization method [54] is employed. After obtaining the optimal hyperparameters, many independent trainings are conducted with data shuffling. In the end, the model with the best performance on the validation data is selected. Fig. 5 presents one of the loss curves during the training and validation process for GHI estimation at BON.

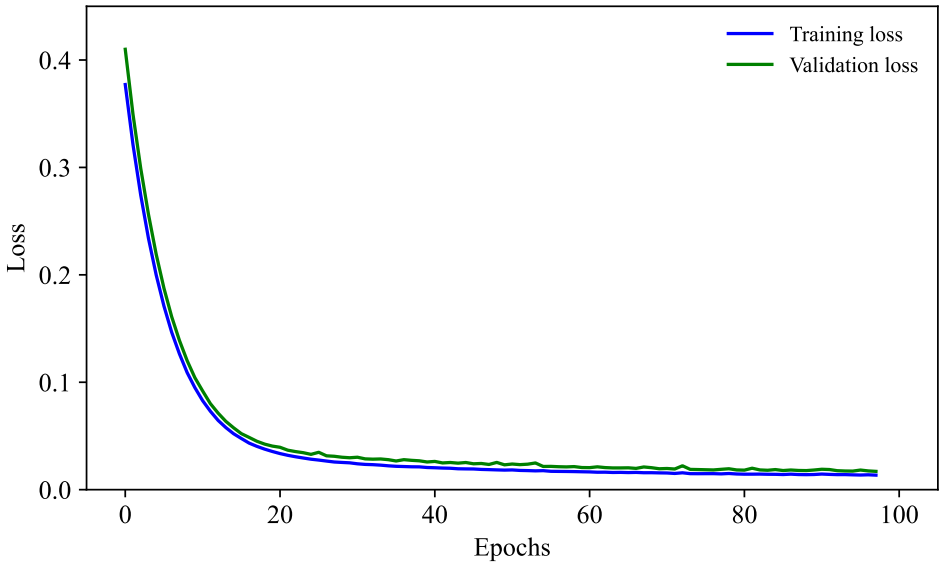

Figure 5: The loss curves of training and validation process for GHI estimation at BON.

The error evaluation metrics are root mean squred error (RMSE), mean bias error (MBE), and their normalized counterparts (nRMSE, nMBE) defined by the following equations:

$$\text{RMSE} = \sqrt{\frac{1}{N}\sum(e_i - o_i)^2}$$

$$\text{nRMSE} = \frac{\sqrt{\frac{1}{N}\sum(e_i - o_i)^2}}{\frac{1}{N}\sum o_i}$$

$$\text{MBE} = \frac{1}{N}\sum(e_i - o_i)$$

$$\text{nMBE} = \frac{\sum(e_i - o_i)}{\sum o_i}$$

where e_i and o_i are the pair of irradiance estimation and ground observation (i.e., GHI or DNI), N is the total number of compared data points.

3. Results

To evaluate the effectiveness of satellite bands selection from correlation analysis, we compare the performance of GHI and DNI estimations based on the proposed deep learning network (without the attention layer) using

satellite images of 16 bands (referred as DNN16 model) and 8 selected bands (referred as DNN8 model). Similarly, to assess the application of attention mechanism in processing satellite images, the results of deep learning model with attention layer (referred as DNNa8 model) are also included in the comparisons in Section 3.1, where the reference is the irradiance estimations from NSRDB. As clouds are the dominant factor affecting the available solar irradiance on the ground level, the comparisons of irradiance estimations of the deep learning model and NSRDB are detailed in clear and cloudy periods in Section 3.2. While a further error analysis of irradiance estimation within different clear-sky index intervals is presented in Section 3.3.

3.1. Comparison of different deep learning networks for irradiance estimations

The irradiance estimation results at SURFRAD stations are presented in Table 3 (for GHI) and Table 4 (for DNI). It is shown in Table 3 that deep learning models for GHI estimations using 16 satellite bands (DNN16) and 8 selected bands (DNN8) have comparable overall performance. DNN16 generates GHI estimations at all the SURFRAD stations with the nRMSE of 20.62% and nMBE of 0.72%, while DNN8 yields a result with slightly larger discrepancies, the nRMSE is 21.17% and the nMBE is -1.97%. When it comes to DNI estimation (see Table 4), the overall results of DNN16 and DNN8 also have limited differences. In specific, the result of DNN16 for DNI estimation has an nRMSE of 24.43% and an nMBE of 0.53%, while DNN8 produces a slightly better result with the nRMSE of 24.36% and the nMBE of 0.44%.

The integration of attention mechanism generally can improve the irrdiance estimations. As shown in Tables 3 and 4, the overall GHI estimation of DNNa8 has a lower nRMSE value of 20.57% than DNN8 (nRMSE of 21.17%), while the nMBE is almost the same (-2.04% vs -1.97%); The DNNa8 model also yields better DNI estimations compared with DNN8, the overall nRMSE is improved from 24.36% to 23.63%, and the nMBE is reduced from 0.44% to 0.36%.

Table 3: The RMSE and MBE in [W m^{-2}], and nRMSE and nMBE in [%], of GHI estimation using different deep learning models at SURFRAD stations. The GHI estimation error of NSRDB is included as the benchmark.

	DNN16[a]		DNN8[b]		DNNa8[c]		NSRDB	
	RMSE (nRMSE)	MBE (nMBE)	RMSE (nRMSE)	MBE (nMBE)	RMSE (nRMSE)	MBE (nMBE)	RMSE (nRMSE)	MBE (nMBE)
BON	89.34 (23.65)	7.53 (1.99)	91.66 (24.26)	8.20 (2.17)	89.13 (23.59)	-9.27 (-2.45)	97.81 (25.89)	-1.28 (-0.34)
DRA	64.64 (12.65)	-5.19 (-1.02)	64.80 (12.68)	-4.62 (-0.90)	66.67 (13.04)	2.83 (0.55)	86.02 (16.83)	-5.05 (-0.99)
FPK	84.44 (22.40)	6.04 (1.60)	87.55 (23.23)	-9.43 (-2.50)	88.65 (23.52)	0.50 (0.13)	105.05 (27.87)	-1.10 (-0.29)
GWN	85.60 (19.30)	9.78 (2.21)	87.88 (19.82)	-14.42 (-3.25)	88.76 (20.02)	-27.58 (-6.22)	107.08 (24.15)	0.18 (0.04)
PSU	97.00 (25.73)	18.97 (5.03)	97.18 (25.78)	-7.35 (-1.95)	91.13 (24.17)	-10.47 (-2.78)	123.42 (32.73)	6.45 (1.71)
SXF	79.57 (20.75)	-15.71 (-4.10)	84.72 (22.09)	-22.12 (-5.77)	80.33 (20.95)	-13.16 (-3.43)	103.12 (26.89)	19.59 (5.11)
TBL	95.84 (22.53)	-0.66 (-0.15)	98.81 (23.22)	-8.75 (-2.06)	92.33 (21.70)	-1.91 (-0.45)	121.47 (28.55)	-0.56 (-0.13)
ALL	85.78 (20.62)	2.98 (0.72)	88.05 (21.17)	-8.18 (-1.97)	85.55 (20.57)	-8.50 (-2.04)	106.96 (25.72)	2.43 (0.58)

[a] 'DNN16' means DNN with inputs of all the 16 channels.

[b] 'DNN8' means DNN with inputs of the 8 selected channels.

[c] 'DNNa8' means DNN with attention layer using the 8 selected channels.

Compared with the GHI and DNI estimations from NSRDB, deep learning based models show substantial improvements as shown in Tables 3 and 4. GHI estimation using DNNa8 reduces the nRMSE by 5.15% from

25.72% to 20.57%, while the bias turns to be enlarged from 0.58% to -2.04%. While for DNI estimation, deep learning models show more aggressive improvements. The nRMSE is reduced from 37.40% to 23.63% (a 13.77% reduction) using the DNNa8 model, and the bias decreases from 6.25% to 0.36%.

Table 4: The RMSE and MBE, in [W m^{-2}], nRMSE and nMBE in [%], of DNI estimation using different deep learning models at SURFRAD stations. The DNI estimation error of NSRDB is included as the benchmark.

	DNN16[a]		DNN8[b]		DNNa8[c]		NSRDB	
	RMSE (nRMSE)	MBE (nMBE)	RMSE (nRMSE)	MBE (nMBE)	RMSE (nRMSE)	MBE (nMBE)	RMSE (nRMSE)	MBE (nMBE)
BON	148.26 (26.25)	33.30 (5.90)	143.01 (25.32)	22.45 (3.98)	143.70 (25.44)	-1.07 (-0.19)	214.61 (38.00)	40.72 (7.21)
DRA	124.35 (17.05)	22.69 (3.11)	122.89 (16.85)	19.05 (2.61)	119.28 (16.36)	24.66 (3.38)	185.50 (25.44)	1.75 (0.24)
FPK	178.43 (29.13)	-2.18 (-0.36)	174.16 (28.43)	29.10 (5.64)	165.76 (27.07)	-13.32 (-2.18)	256.06 (41.81)	40.53 (6.62)
GWN	129.80 (22.40)	-23.11 (-3.99)	133.64 (23.06)	-27.88 (-4.81)	123.81 (21.37)	3.88 (0.67)	200.48 (34.60)	40.12 (6.92)
PSU	163.44 (29.90)	-28.28 (-5.17)	165.87 (30.34)	-30.22 (-5.53)	161.80 (29.60)	5.09 (0.93)	245.39 (44.89)	50.07 (9.16)
SXF	147.58 (25.68)	21.84 (3.80)	149.16 (25.95)	19.43 (3.38)	143.46 (24.96)	-6.33 (-1.10)	253.93 (44.18)	73.79 (12.84)
TBL	156.15 (25.90)	-6.82 (-1.13)	156.45 (25.95)	-11.80 (-1.96)	154.95 (25.70)	-7.36 (-1.22)	247.34 (41.02)	37.57 (6.23)
ALL	148.69 (24.43)	3.24 (0.53)	148.26 (24.36)	2.66 (0.44)	143.84 (23.63)	2.20 (0.36)	227.61 (37.40)	38.04 (6.25)

[a] 'DNN16' means DNN with inputs of all the 16 channels.

[b] 'DNN8' means DNN with inputs of the 8 selected channels.

[c] 'DNNa8' means DNN with attention layer using the 8 selected channels.

3.2. Comparison under clear and cloudy sky conditions

Since the cloud is the primary atmospheric constitute affecting the available solar irradiance on the ground level, solar resource assessment under cloudy sky conditions is generally associated with larger uncertainties in both semi-empirical and physical satellite-based methods [19]. Therefore, it might be of interest to evaluate the performance of deep learning based model for solar irradiance (i.e., GHI and DNI) estimation under cloudy and clear sky conditions that are based on Bright-Sun clear-sky detection algorithm [38].

The overall performance of GHI and DNI estimations using deep learning model (DNNa8) and physical solar model (NSRDB) are presented in Tables 5 and 6. As shown in Table 5, GHI estimation of DNNa8 has larger discrepancies than NSRDB in clear sky periods. In specific, DNNa8 has a RMSE of 39.88 W m^2 and a MBE of -9.78 W m^2, while the RMSE and MBE of NSRDB are 27.09 W m^2 and 2.15 W m^2, respectively. In cloudy sky periods, GHI estimates of DNNa8 show better performance than NSRDB in terms of nRMSE with the reduction of 6.92% from 32.48% to 25.56%, while the bias becomes larger from 0.68% to -2.22%. As for DNI estimation (see Table 6), DNNa8 typically shows better results than NSRDB with the exception of a larger bias in clear sky periods. Compared with NSRDB for estimating DNI in clear skies, DNNa8 reduces the RMSE from 85.43 W m^2 to 73.55 W m^2, while the MBE is enlarged from -12.28 W m^2 to -20.23 W m^2. When the sky is cloudy, the DNI estimation of NSRDB has a RMSE of 263.85 W m^2 and the MBE is 58.17 W m^2. DNNa8 yields an estimation with the errors of RMSE and MBE decreased to 163.73 W m^2 and 11.18 W m^2, respectively. The results of GHI and DNI estimation on some selected days are presented in Fig. 6 for clear, cloudy, and partially cloudy days. It is shown that both GHI and DNI of DNNa8 have lower divergences compared with NSRDB in cloudy periods.

Table 5: The comparison of GHI estimation results under clear and cloudy periods at all SURFRAD stations using deep learning (DNNa8) and physical solar model (NSRDB).

	DNNa8				NSRDB			
	RMSE [W m^{-2}]	nRMSE [%]	MBE [W m^{-2}]	nMBE [%]	RMSE [W m^{-2}]	nRMSE [%]	MBE [W m^{-2}]	nMBE [%]
Clear periods	39.88	6.65	-9.78	-1.63	27.09	4.52	2.15	0.36
Cloudy periods	93.94	25.56	-8.16	-2.22	119.40	32.48	2.50	0.68
All periods	85.55	20.57	-8.18	-2.04	106.96	25.72	2.43	0.58

Table 6: The comparison of DNI estimation results under clear and cloudy periods at all SURFRAD stations using deep learning (DNNa8) and physical solar model (NSRDB).

	DNNa8				NSRDB			
	RMSE [W m^{-2}]	nRMSE [%]	MBE [W m^{-2}]	nMBE [%]	RMSE [W m^{-2}]	nRMSE [%]	MBE [W m^{-2}]	nMBE [%]
Clear periods	73.55	8.40	-20.23	-2.31	85.43	9.76	-12.28	-1.40
Cloudy periods	163.73	32.62	11.18	-2.22	263.85	52.59	58.17	11.59
All periods	143.84	23.63	2.20	0.36	227.61	37.40	38.04	6.25

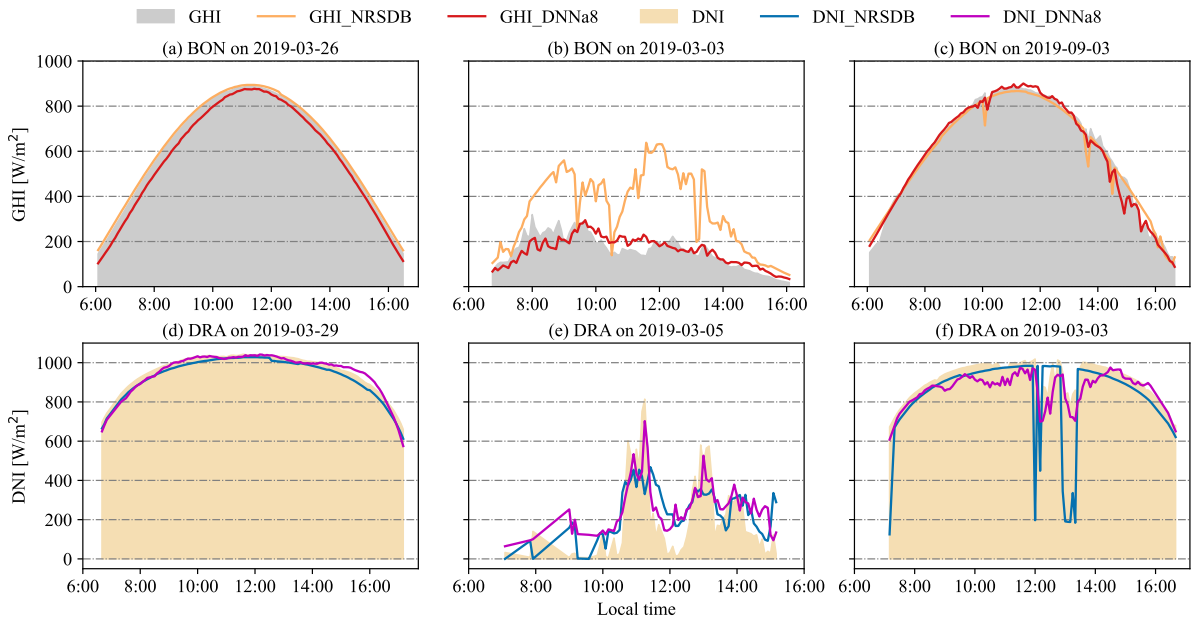

Figure 6: GHI and DNI estimation results on some selected days at BON and DRA. (a) and (d) are on clear days, (b) and (e) are on cloudy days, while (c) and (f) are for partially cloudy days.

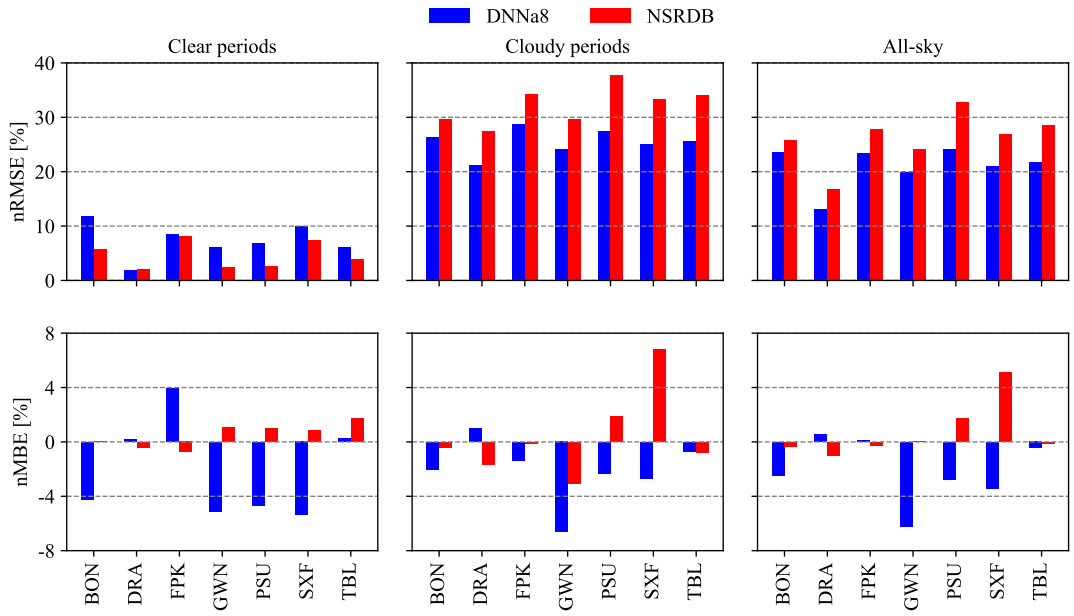

Figure 7: The comparison of GHI estimation using deep learning (DNNa8) and physical solar model (NSRDB) under clear, cloudy, all-sky conditions at all SURFRAD stations.

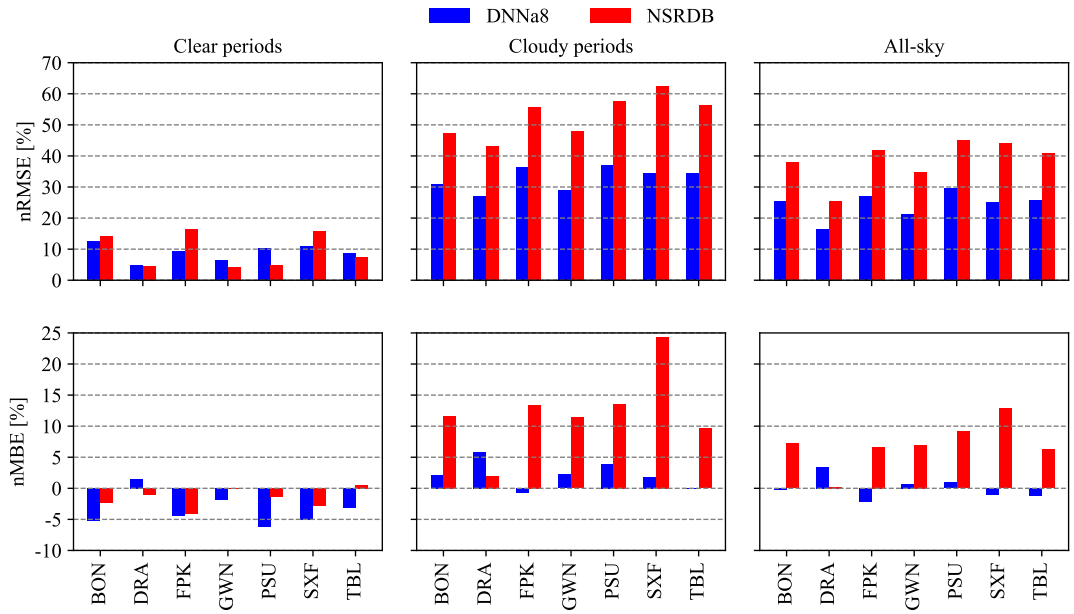

Figure 8: The comparison of DNI estimation using deep learning (DNNa8) and physical solar model (NSRDB) under clear, cloudy, all-sky conditions at all SURFRAD stations.

Fig. 7 presents the detailed comparison of GHI estimation at all SURFRAD stations using deep learning and physical model. Compared with NSRDB, DNNa8 generally produces lower RMSE in cloudy and all-sky conditions, while the RMSE value in clear periods is higher. DNNa8 turns to generates comparatively larger negative bias for both clear and cloudy periods (e.g., BON, GWN, and PSU). The site-specific comparison of DNI estimation is shown in Fig. 8. Generally, deep learning model outperforms the physical model in cloudy sky

conditions with lower values of RMSE and MBE. Similarly, DNNa8 is more likely to yield DNI estimation with larger biases in clear periods.

3.3. Error analysis

To further evaluate the results of solar irradiance estimations using deep learning based method, we herein compare the performance with physical model in NSRDB within different clear-sky index intervals based on the Ineichen-Perez model. Since the intervals of clear-sky index are determined for GHI and DNI separately, the error analysis is performed in each clear-sky index intervals for both GHI and DNI estimations. Note that the use of other clear-sky models, e.g., McClear [55] or REST2 [56] has similar results, as the aim is to evaluate the performance of GHI and DNI estimations under various conditions.

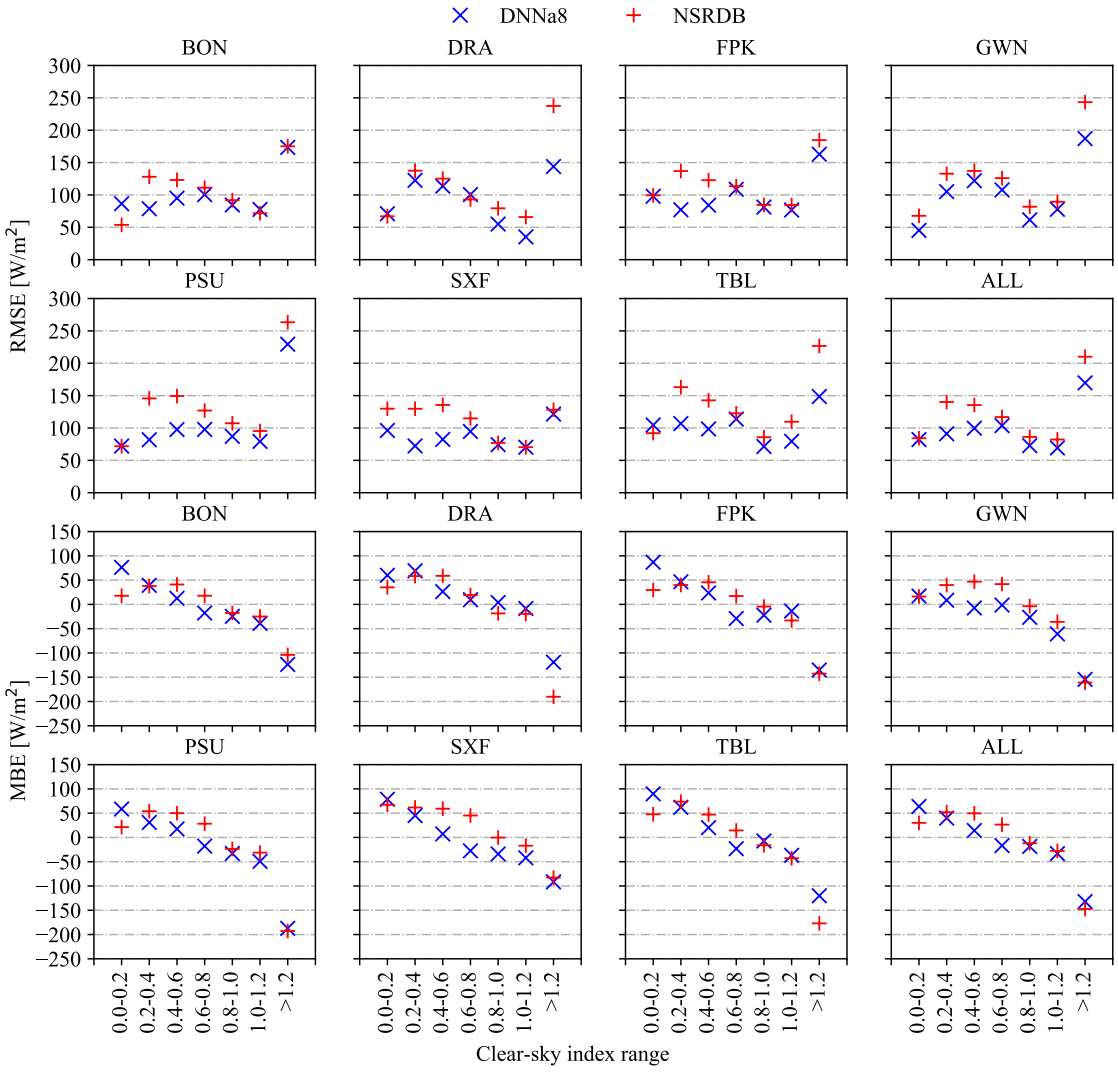

Figure 9: The comparison of GHI estimation using deep learning (DNNa8) and physical solar model (NSRDB) across clear-sky index intervals at all SURFRAD stations. 'ALL' means all the stations are included.

A detailed comparison of GHI estimation in different clear-sky index intervals at all SURFRAD stations is presented in Fig. 9. Generally, DNNa8 is more likely to produce GHI estimation with lower discrepancies (also

see Fig. A1 for the joint and marginal distributions for GHI measurements and estimations, and Fig. A2 for error distributions). Both DNNa8 and NSRDB generate overestimation in the conditions of low clear-sky index and underestimation when the clear-sky index is high, especially when the clear-sky index exceeds 1.2 as shown in Fig. 9. Moreover, DNNa8 and NSRDB also exhibit high divergences in GHI estimation when the clear-sky index is higher than 1.2.

Fig. 10 presents the comparison of DNI estimation in different clear-sky intervals at all SURFRAD stations. The overall trend is that both deep learning and physical model yield DNI estimations with lower RMSE values when the clear-sky index increases. Meanwhile, DNI is generally overestimated when the clear-sky index is low and underestimated for high clear-sky indexes, the bias exhibits a linear approximation and decreases from positive to negative with the increase of clear-sky index. Despite some on-site variations, for instance, high RMSE when clear-sky index exceeds 1.2 (i.e., DRA and FPK), larger divergences of DNNa8 (e.g., at GWN and PSU when clear-sky index is greater than 1.2), deep learning generally outperforms physical model (see Fig. A3 for the joint and marginal distributions for DNI measurements and estimations, and Fig. A4 for error distributions).

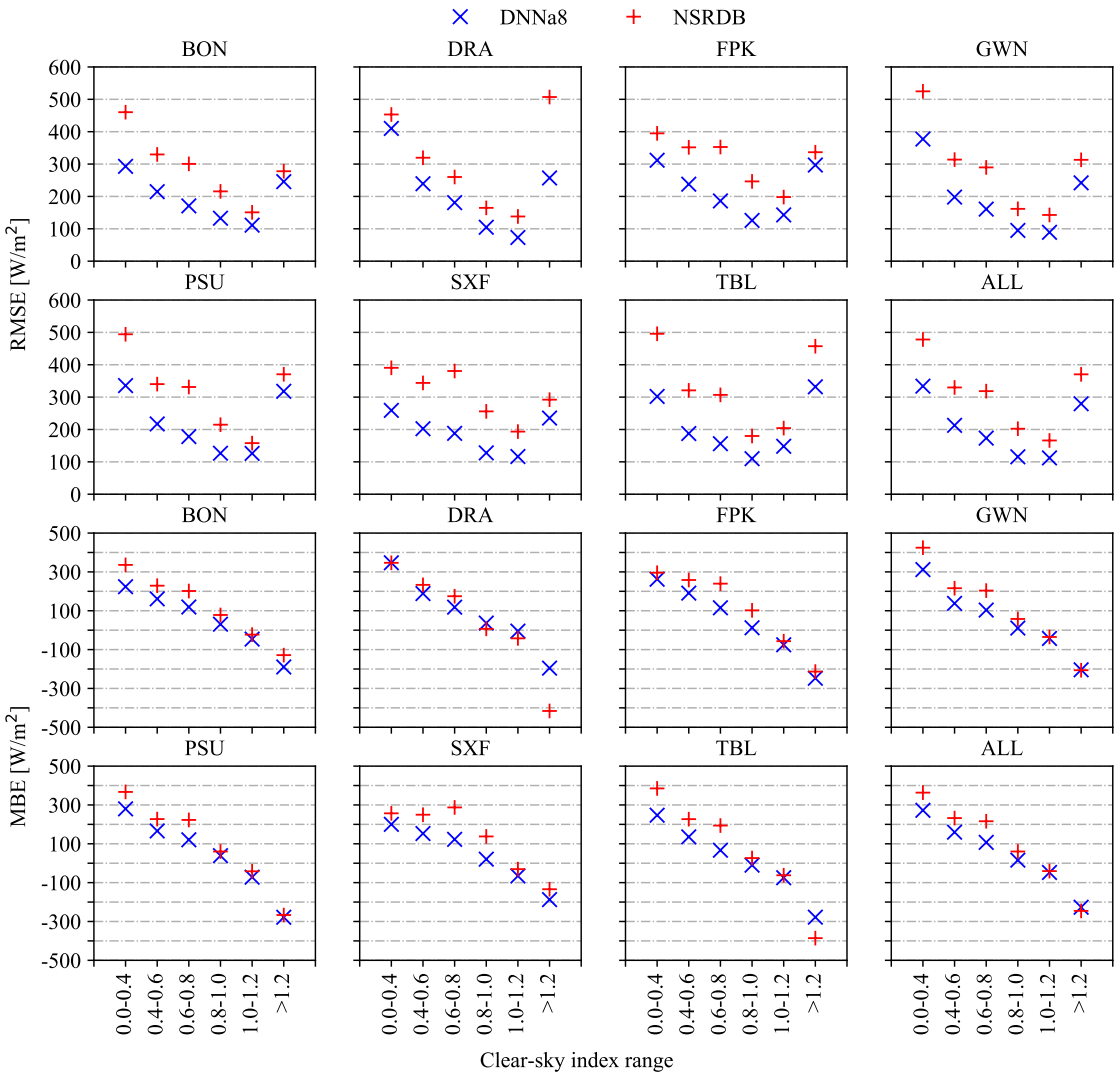

Figure 10: The comparison of DNI estimation using deep learning (DNNa8) and physical solar model (NSRDB) across clear-sky index intervals at all SURFRAD stations.'ALL' means all the stations are included.

4. Discussion

Based on the results of DNN16 and DNN8, correlation analysis is effective to select the representative satellite bands to support solar irradiance modeling. Note that although the results of DNN16 and DNN08 show some site-specific variations as detailed in Tables 3 and 4, the overall picture is that divergences between DNN16 and DNN8 remain insignificant. This means the information in the sub-selected bands is still sufficient to infer the atmospheric compositions attenuating solar radiation. Therefore, it can reduce the complexity and improve the efficiency in retrieving solar irradiance using satellite data, especially for regional applications with long-time period. Similarly, based on the results of DNN8 and DNNa8, the attention layer generally shows positive impact for irradiance estimation. However, the improvement is not significant. The possible reason is that the attention mechanism is to extract information on a sub-target area rather than the whole domain, and the ground station is located on the centered pixel in relatively small images. Therefore, the attention mechanism can not outperform too much than the baseline model. Since NSRDB employs physical solar model and reanalysis products to simulate the interactions between atmospheric components and solar radiation. The improvements in both GHI and DNI estimations using deep learning and satellite images indicate that deep learning may have the potential to simplify the radiative transfer simulations for solar resource assessment.

When comparing the results in clear and cloudy periods, DNNa8 generally turns to produce larger biases for GHI estimations in both clear and cloudy sky conditions and therefore underestimates in the overall results (see Table 5). Nevertheless, the improvements of deep learning based model for estimating GHI in cloudy conditions are noticeable. Consequently, the overall RMSE of all-sky GHI estimation of DNNa8 is smaller than NSRDB. As for DNI estimation, DNNa8 outperforms NSRDB for all-sky conditions. Since DNI is more sensitive than GHI to the attenuating effect of atmospheric constitutes, the estimation of DNI is more challenging, evidenced by the generally larger variances and biases produced by both deep learning and physical models (see Table 6). Deep learning shows a compromised performance for irradiance estimation in clear sky conditions. The possible reason could be the selected satellite bands are more effective in representing the cloud properties, while the information of atmospheric aerosol and water vapor can not be extracted as accurately as the reanalysis products used in NSRDB, especially under clear sky conditions. Nevertheless, the application of deep learning could improve the overall performance of solar resource assessment inferring satellite measurements compared to the physical solar model in NSRDB. The improvements in GHI and DNI estimations might be beneficial to the solar community.

For the high discrepancies observed in Fig. 9 when clear-sky index is greater than 1.2, the possible explanation could be the cloud enhancement effect [57]. Cloud enhancements can cause the GHI to instantaneously exceed the clear-sky GHI and even the solar constant [9]. As shown in Fig. 11, the measured GHI can be greater than the projection of extraterrestrial radiation on the horizontal surface with high fluctuations due to cloud enhancement. Therefore, the clear-sky index is expected to be greater than 1.0. However, the cloud enhancement is rather an instantaneous process, satellite sensors might not be able to capture these phenomena. Satellite-based deep learning and physical methods could not obtain accurate GHI estimation when cloud enhancement happens, which is the major contributor for the relatively larger errors (i.e., underestimation) when the clear-sky index is greater than 1.2. Meanwhile, deep learning still faces challenges in retrieving DNI via satellite images under cloudy conditions (low clear-sky index, see Fig. 9), where the errors are comparatively larger. Although DNI estimation is generally with larger uncertainties, deep learning shows potential especially in extracting cloud information

via satellite images. To further improve the accuracy of solar irradiance estimation, cloud enhancements on GHI should be better accounted for. While for DNI, more sophisticated methods to reveal the cloud affecting direct solar rays should be developed.

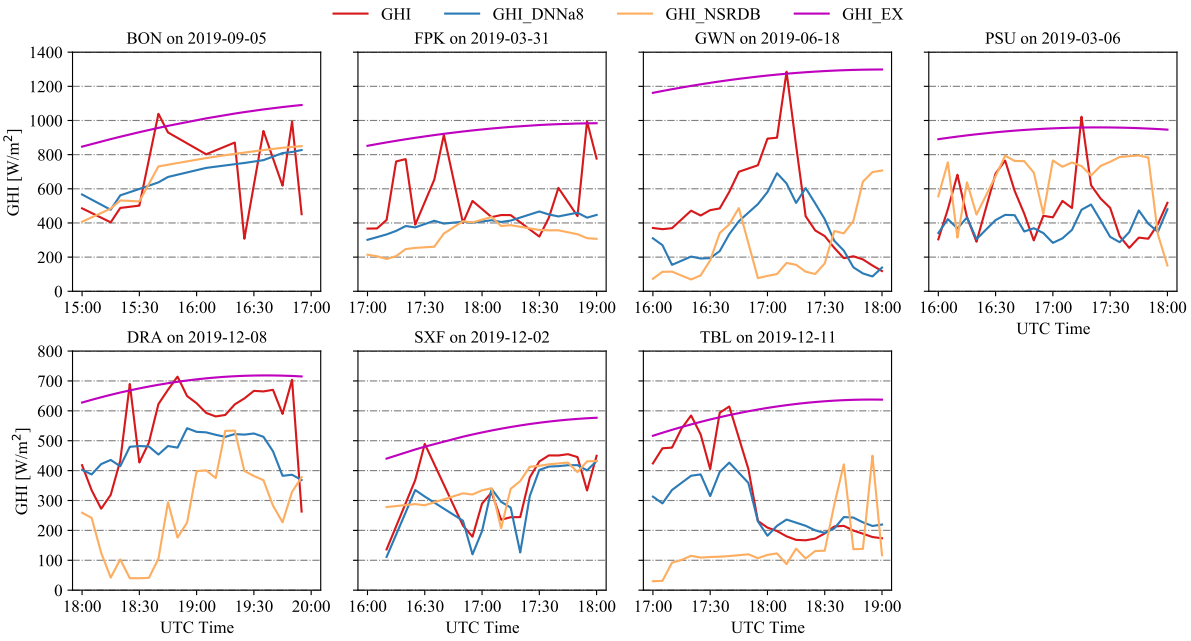

Figure 11: The cloud enhancement events at the SURFRAD stations. GHI is the actual measurement, GHI_DNNa8 and GHI_NSRDB are the estimations from the deep learning model and physical solar model, respectively. GHI_EX is the extraterrestrial radiation projected on the horizontal surface.

5. Conclusions

The 16 spectral channels of GOES-16 can be used individually or together to reveal atmospheric characteristics for various applications. In this work, multispectral GOES-16 images are used for estimating solar irradiance (i.e., GHI and DNI) by deep learning. After pre-processing, a correlation analysis is applied to select the representative bands. The satellite images of selected bands are then used as inputs for a deep learning model based on convolutional, attention, and dense layers. Clear-sky indexes are used as the labels for both GHI and DNI estimation models. The performance of the proposed methods and the effectiveness of bands selection are evaluated against the measurements and compared with irradiance estimations from NSRDB.

Deep learning models based on 16 spectral bands (DNN16) and 8 selected bands (DNN8) have comparable performance for both GHI and DNI estimations compared to the ground measurements at SURFRAD stations. This demonstrates the effectiveness of correlation analysis in selecting representative spectral satellite bands for solar irradiance estimation. It is more effective to use a subset of satellite spectral bands to reduce model complexity and computational cost, which is especially beneficial for large-scale applications.

Furthermore, the integration of attention mechanism in deep learning (DNNa8) shows improvements in both GHI and DNI estimations. When compared with NSRDB, DNNa8 generally produces GHI estimation with lower RMSE in cloudy conditions, but higher RMSE in cloudless skies. Nevertheless, the improvements in GHI estimation under cloudy conditions lead to an overall nRMSE reduction of 5.15%. Similarly, the overall nRMSE for

DNI estimations is reduced from 37.40% to 23.63%, and the bias is improved from 6.25% to 0.36%. Satellite images provide more spatial information (i.e., nonlocal cloud) around the target location than a single pixel, and the attention mechanism enables the model focus on more important features. As a result, both GHI and DNI estimations show improvements, especially in cloudy conditions. This means the attention mechanism might be applicable for solar irradiance estimation over a larger area given on-site data available.

When comparing DNNa8 and NSRDB in irradiance estimations across different ranges of clear-sky index, deep learning models still show better overall performance in both GHI and DNI estimations. That said, both GHI and DNI estimations with improved accuracy via deep learning might provide more benefits in solar irradiance modeling. It is necessary to mention that both satellite-based deep learning and physical models could not account for the cloud enhancement effects, where comparatively larger errors are observed for GHI estimation when the clear-sky index exceeds 1.2. Although deep learning performs comparatively better than physical models in extracting cloud information, more efforts are still needed for revealing the cloud properties across the vertical atmospheric layers.

In summary, correlation analysis is effective in selecting representative satellite bands to reduce the complexity and improve the efficiency in solar irradiance estimation. Although deep learning with attention mechanism provides an alternative for satellite-to-irradiance methods, there are still some limitations, such as the need of ground measurements for model development and the incapability in capturing cloud enhancement events. Notwithstanding, the combination of deep learning and remote sensing shows potential in extracting cloud information via satellite images. The high spatiotemporal resolution satellite-to-irradiance data with improved accuracy can better capture the solar variability, which is beneficial for designing solar energy projects.

Acknowledgement

The authors gratefully acknowledge the partial support from the Hong Kong Polytechnic University Grant P0035016, and the partial support from Hong Kong University Grants Committee (UGC) Grant 25213022.

Appendix

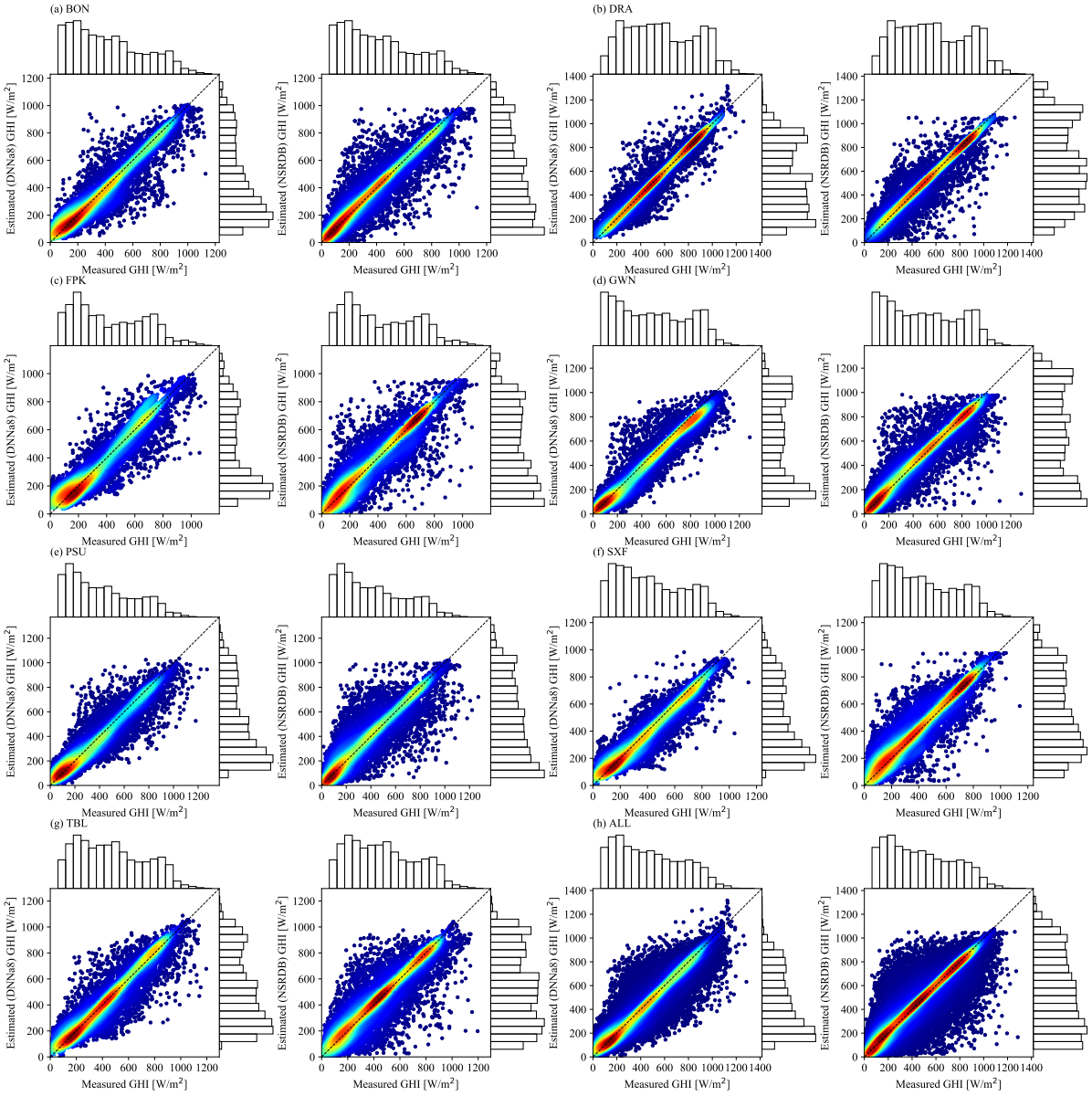

Figure A1: Joint and marginal distributions for GHI measurements and estimations of DNNa8 and NSRDB at all SURFRAD stations: (a) BON, (b) DRA, (c) FPK, (d) GWN, (e) PSU, (f) SXF, (g) TBL, (h) ALL. 'ALL' means all the stations are included. The colors show 2D kernel densities. GHI estimations of DNNa8 generally show better agreements with GHI observations than NSRDB.

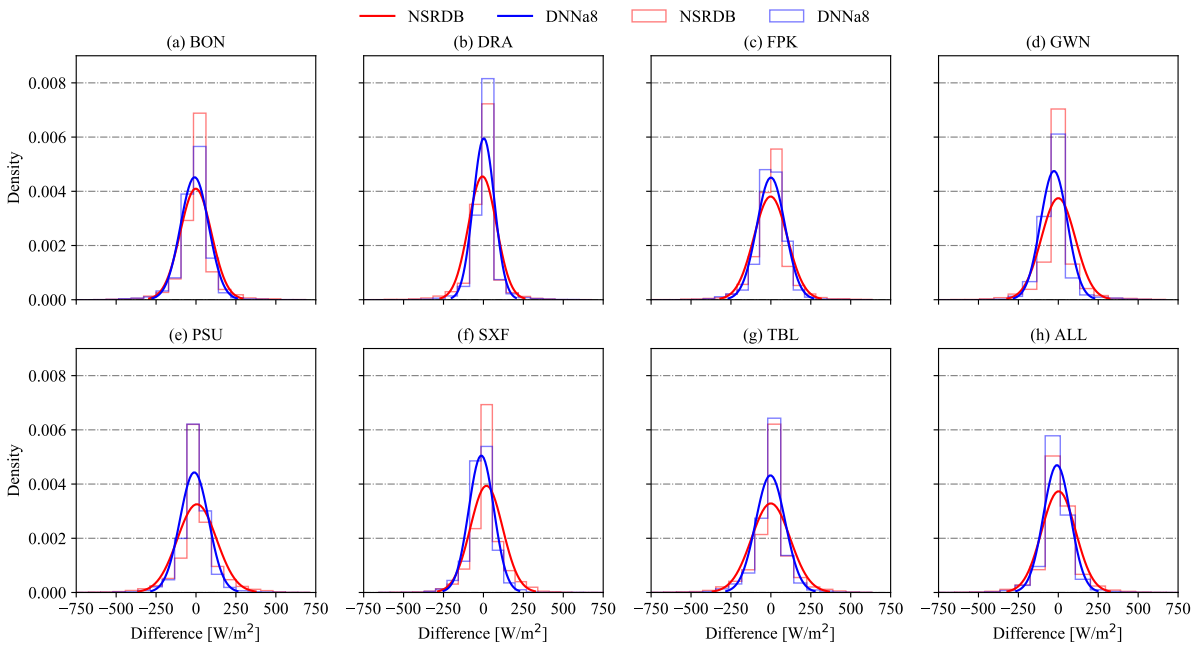

Figure A2: The error distributions for GHI estimations of DNNa8 and NSRDB at all the SURFRAD stations: (a) BON, (b) DRA, (c) FPK, (d) GWN, (e) PSU, (f) SXF, (g) TBL, (h) ALL. 'ALL' means all the stations are included. The density is a normalized probability density, the error is the difference between DNI estimate and measurement. A gaussian regression is performed for each distribution. The error of DNNa8 shows a narrower profile compared with NSRDB.

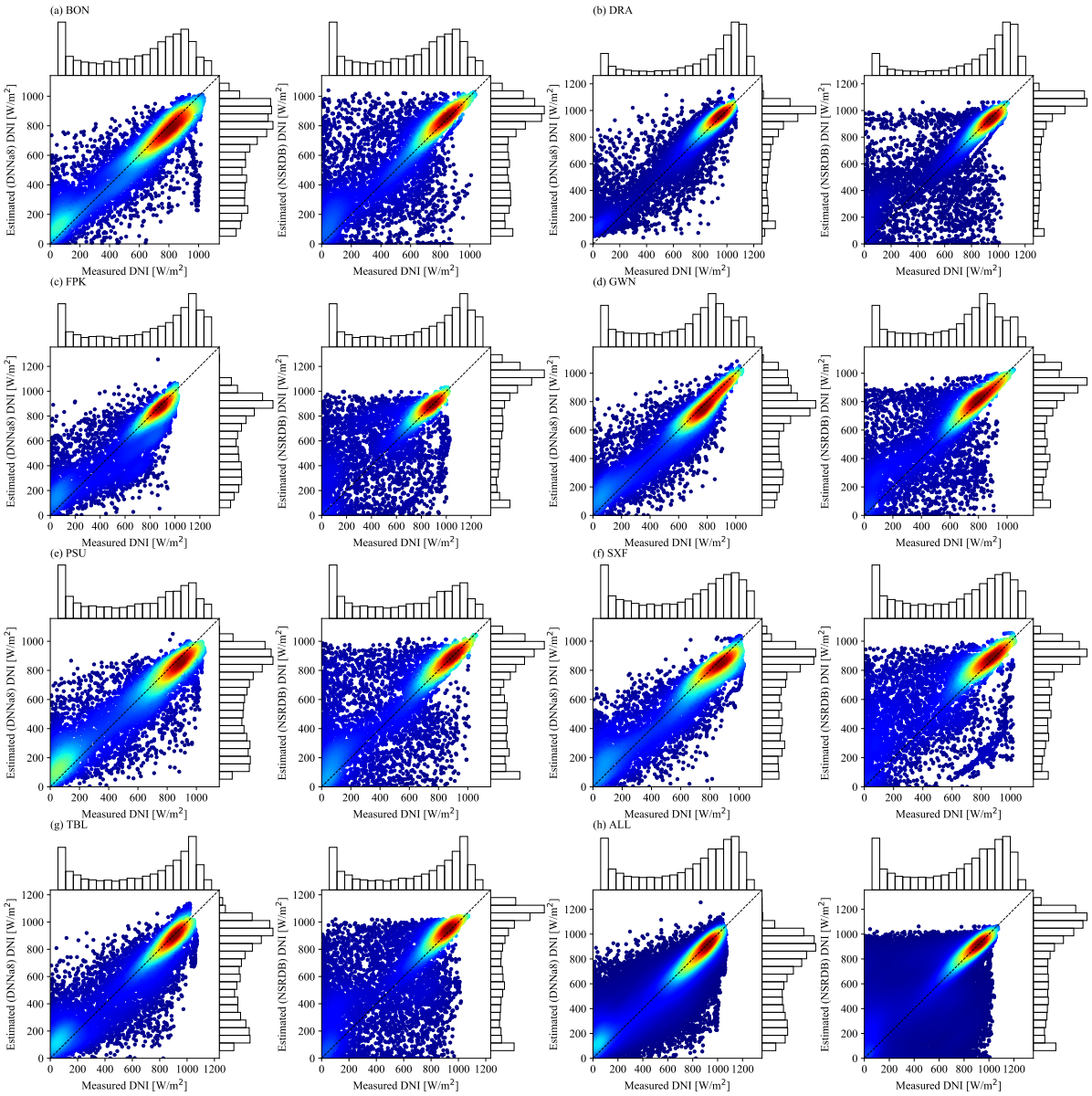

Figure A3: Joint and marginal distributions for DNI measurements and estimations of DNNa8 and NSRDB at all SURFRAD stations: (a) BON, (b) DRA, (c) FPK, (d) GWN, (e) PSU, (f) SXF, (g) TBL, (h) ALL. 'ALL' means all the stations are included. The colors show 2D kernel densities. DNI estimations of DNNa8 generally show better agreements with DNI observations than NSRDB.

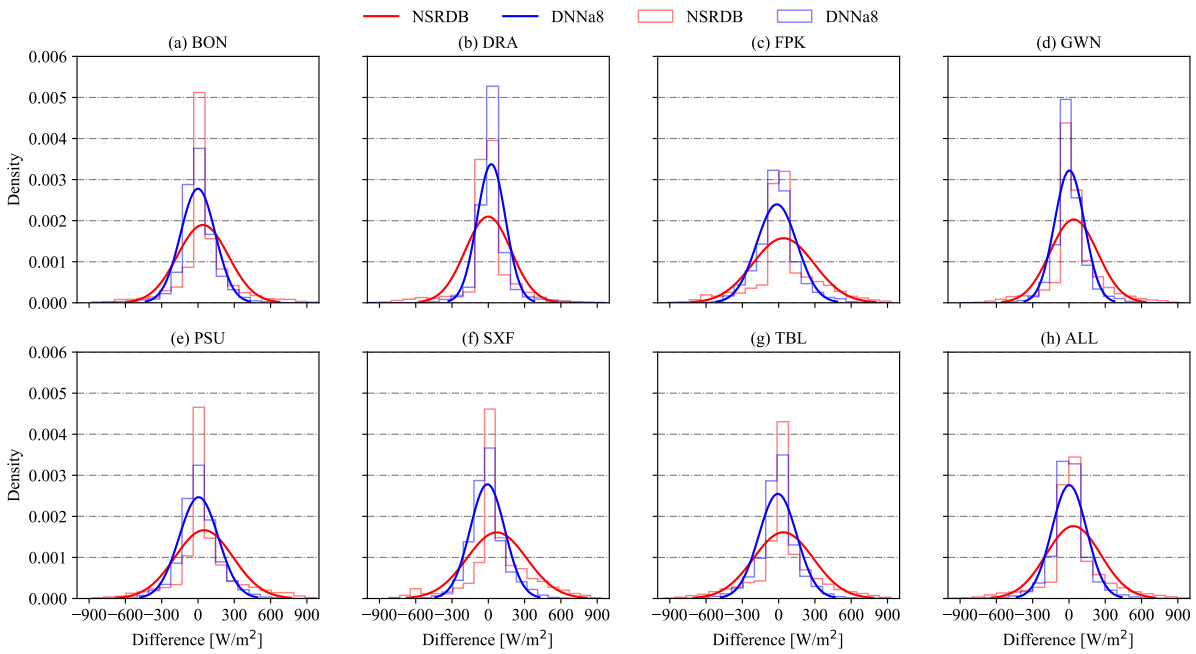

Figure A4: The error distributions for DNI estimations of DNNa8 and NSRDB at all the SURFRAD stations: (a) BON, (b) DRA, (c) FPK, (d) GWN, (e) PSU, (f) SXF, (g) TBL, (h) ALL. 'ALL' means all the stations are included. The density is a normalized probability density, the error is the difference between DNI estimate and measurement. A gaussian regression is performed for each distribution. The error of DNNa8 shows a narrower profile compared with NSRDB.

References

[1] IEA, World Energy Outlook 2021 [online], Available at: https://www.iea.org/reports/world-energy-outlook-2021, (Accessed on 04/08/2022) (2021).

[2] D. Yang, W. Wang, C. A. Gueymard, T. Hong, J. Kleissl, J. Huang, M. J. Perez, R. Perez, J. M. Bright, X. Xia, et al., A review of solar forecasting, its dependence on atmospheric sciences and implications for grid integration: Towards carbon neutrality, Renewable and Sustainable Energy Reviews 161 (2022) 112348.

[3] IEA, Renewables 2021 [online], Available at: https://www.iea.org/reports/renewables-2021, (Accessed on 04/08/2022) (December 2021).

[4] IEA, Solar PV [online], Available at: https://www.iea.org/reports/solar-pv, (Accessed on 04/08/2022) (November 2021).

[5] IEA, Concentrated Solar Power (CSP) [online], Available at: https://www.iea.org/reports/concentrated-solar-power-csp, (Accessed on 04/08/2022) (November 2021).

[6] J. Kleissl, Solar energy forecasting and resource assessment, Academic Press, 2013.

[7] Y. Chu, M. Li, C. F. M. Coimbra, D. Feng, H. Wang, Intra-hour irradiance forecasting techniques for solar power integration: A review, iScience (2021) 103136.

[8] Y. Chu, M. Li, C. F. M. Coimbra, Sun-tracking imaging system for intra-hour DNI forecasts, Renewable Energy 96 (2016) 792–799.

[9] R. H. Inman, Y. Chu, C. F. M. Coimbra, Cloud enhancement of global horizontal irradiance in California and Hawaii, Solar Energy 130 (2016) 128–138.

[10] M. Li, Y. Chu, H. T. C. Pedro, C. F. M. Coimbra, Quantitative evaluation of the impact of cloud transmittance and cloud velocity on the accuracy of short-term DNI forecasts, Renewable Energy 86 (2016) 1362–1371.

[11] D. Yang, W. Wang, X. Xia, A concise overview on solar resource assessment and forecasting, Advances in Atmospheric Sciences (2022) 1–13.

[12] G. M. Yagli, D. Yang, O. Gandhi, D. Srinivasan, Can we justify producing univariate machine-learning forecasts with satellite-derived solar irradiance?, Applied Energy 259 (2020) 114122.

[13] A. F. Zambrano, L. F. Giraldo, Solar irradiance forecasting models without on-site training measurements, Renewable Energy 152 (2020) 557–566.

[14] G. Salazar, C. Gueymard, J. B. Galdino, O. de Castro Vilela, N. Fraidenraich, Solar irradiance time series derived from high-quality measurements, satellite-based models, and reanalyses at a near-equatorial site in Brazil, Renewable and Sustainable Energy Reviews 117 (2020) 109478.

[15] B. Babar, L. T. Luppino, T. Boström, S. N. Anfinsen, Random forest regression for improved mapping of solar irradiance at high latitudes, Solar Energy 198 (2020) 81–92.

[16] G. Huang, Z. Li, X. Li, S. Liang, K. Yang, D. Wang, Y. Zhang, Estimating surface solar irradiance from satellites: Past, present, and future perspectives, Remote Sensing of Environment 233 (2019) 111371.

[17] M. Sengupta, Y. Xie, A. Lopez, A. Habte, G. Maclaurin, J. Shelby, The National Solar Radiation Database (NSRDB), Renewable and Sustainable Energy Reviews 89 (2018) 51–60.

[18] Z. Qu, A. Oumbe, P. Blanc, B. Espinar, G. Gesell, B. Gschwind, L. Klüser, M. Lefèvre, L. Saboret, M. Schroedter-Homscheidt, Fast radiative transfer parameterisation for assessing the surface solar irradiance: The Heliosat-4 method, Meteorologische Zeitschrift 26 (1) (2017) 33–57.

[19] S. Chen, Z. Liang, S. Guo, M. Li, Estimation of high-resolution solar irradiance data using optimized semi-empirical satellite method and GOES-16 imagery, Solar Energy 241 (2022) 404–415.

[20] M. Sengupta, A. Habte, S. Wilbert, C. Gueymard, J. Remund, Best practices handbook for the collection and use of solar resource data for solar energy applications, Tech. rep., National Renewable Energy Lab.(NREL), Golden, CO (United States) (2021).

[21] J. Polo, S. Wilbert, J. A. Ruiz-Arias, R. Meyer, C. Gueymard, M. Suri, L. Martin, T. Mieslinger, P. Blanc, I. Grant, et al., Preliminary survey on site-adaptation techniques for satellite-derived and reanalysis solar radiation datasets, Solar Energy 132 (2016) 25–37.

[22] M. A. Hassan, A. Khalil, S. Kaseb, M. A. Kassem, Exploring the potential of tree-based ensemble methods in solar radiation modeling, Applied Energy 203 (2017) 897–916.

[23] L. Cornejo-Bueno, C. Casanova-Mateo, J. Sanz-Justo, S. Salcedo-Sanz, Machine learning regressors for solar radiation estimation from satellite data, Solar Energy 183 (2019) 768–775.

[24] F. Liu, X. Wang, F. Sun, H. Wang, Correct and remap solar radiation and photovoltaic power in china based on machine learning models, Applied Energy 312 (2022) 118775.

[25] H. Jiang, N. Lu, J. Qin, W. Tang, L. Yao, A deep learning algorithm to estimate hourly global solar radiation from geostationary satellite data, Renewable and Sustainable Energy Reviews 114 (2019) 109327.

[26] A. Nespoli, A. Niccolai, E. Ogliari, G. Perego, E. Collino, D. Ronzio, Machine learning techniques for solar irradiation nowcasting: Cloud type classification forecast through satellite data and imagery, Applied Energy 305 (2022) 117834.

[27] G. Notton, C. Voyant, A. Fouilloy, J. L. Duchaud, M. L. Nivet, Some applications of ANN to solar radiation estimation and forecasting for energy applications, Applied Sciences 9 (1) (2019) 209.

[28] N. Lu, J. Qin, K. Yang, J. Sun, A simple and efficient algorithm to estimate daily global solar radiation from geostationary satellite data, Energy 36 (5) (2011) 3179–3188.

[29] P. Verma, S. Patil, A machine learning approach and methodology for solar radiation assessment using multispectral satellite images, Annals of Data Science (2021) 1–26.

[30] J. Chen, W. Zhu, Q. Yu, Estimating half-hourly solar radiation over the Continental United States using GOES-16 data with iterative random forest, Renewable Energy 178 (2021) 916–929.

[31] J. Chen, W. Zhu, Q. Yu, High-spatiotemporal-resolution estimation of solar energy component in the united states using a new satellite-based model, Journal of Environmental Management 302 (2022) 114077.

[32] P. A. C. Rocha, V. O. Santos, Global horizontal and direct normal solar irradiance modeling by the machine learning methods XGBoost and deep neural networks with CNN-LSTM layers: a case study using the goes-16 satellite imagery, International Journal of Energy and Environmental Engineering (2022) 1–16.

[33] D. Yang, Validation of the 5-min irradiance from the National Solar Radiation Database (NSRDB), Journal of Renewable and Sustainable Energy 13 (1) (2021) 016101.

[34] A. Vaswani, N. Shazeer, N. Parmar, J. Uszkoreit, L. Jones, A. N. Gomez, Ł. Kaiser, I. Polosukhin, Attention is all you need, Advances in neural information processing systems 30.

[35] P. Ineichen, R. Perez, A new airmass independent formulation for the Linke turbidity coefficient, Solar Energy 73 (3) (2002) 151–157.

[36] W. F. Holmgren, C. W. Hansen, M. A. Mikofski, pvlib python: A python package for modeling solar energy systems, Journal of Open

Source Software 3 (29) (2018) 884.

[37] J. A. Augustine, J. J. DeLuisi, C. N. Long, SURFRAD–A national surface radiation budget network for atmospheric research, Bulletin of the American Meteorological Society 81 (10) (2000) 2341–2358.

[38] J. M. Bright, X. Sun, C. A. Gueymard, B. Acord, P. Wang, N. A. Engerer, Bright-Sun: A globally applicable 1-min irradiance clear-sky detection model, Renewable and Sustainable Energy Reviews 121 (2020) 109706.

[39] M. Sengupta, Y. Xie, A. Habte, G. Buster, G. Maclaurin, P. Edwards, H. Sky, M. Bannister, E. Rosenlieb, The national solar radiation database (nsrdb) final report: Fiscal years 2019-2021, Tech. rep., National Renewable Energy Lab.(NREL), Golden, CO (United States) (2022).

[40] G. Chandrashekar, F. Sahin, A survey on feature selection methods, Computers & Electrical Engineering 40 (1) (2014) 16–28.

[41] S.-y. Jiang, L.-x. Wang, Efficient feature selection based on correlation measure between continuous and discrete features, Information Processing Letters 116 (2) (2016) 203–215.

[42] M. A. Hall, Correlation-based Feature Selection for Machine Learning, Ph.D. thesis, Citeseer (1999).

[43] L. Yu, H. Liu, Feature selection for high-dimensional data: A fast correlation-based filter solution, in: Proceedings of the 20th international conference on machine learning (ICML-03), 2003, pp. 856–863.

[44] P. Kumari, D. Toshniwal, Deep learning models for solar irradiance forecasting: A comprehensive review, Journal of Cleaner Production 318 (2021) 128566.

[45] I. Goodfellow, Y. Bengio, A. Courville, Deep learning, MIT press, 2016.

[46] C. Feng, J. Zhang, Solarnet: A sky image-based deep convolutional neural network for intra-hour solar forecasting, Solar Energy 204 (2020) 71–78.

[47] M. Ajith, M. Martínez-Ramón, Deep learning based solar radiation micro forecast by fusion of infrared cloud images and radiation data, Applied Energy 294 (2021) 117014.

[48] J. Zhang, J. Wu, H. Wang, Y. Wang, Y. Li, Cloud detection method using CNN based on cascaded feature attention and channel attention, IEEE Transactions on Geoscience and Remote Sensing 60 (2021) 1–17.

[49] Z. Niu, G. Zhong, H. Yu, A review on the attention mechanism of deep learning, Neurocomputing 452 (2021) 48–62.

[50] M. Abadi, A. Agarwal, P. Barham, E. Brevdo, Z. Chen, C. Citro, G. S. Corrado, A. Davis, J. Dean, M. Devin, et al., Tensorflow: Large-scale machine learning on heterogeneous distributed systems, arXiv preprint arXiv:1603.04467.

[51] S. Chen, M. Li, Improved turbidity estimation from local meteorological data for solar resourcing and forecasting applications, Renewable Energy 189 (2022) 259–272.

[52] S. Chen, Z. Liang, P. Dong, S. Guo, M. Li, A transferable turbidity estimation method for estimating clear-sky solar irradiance, Renewable Energy 206 (2023) 635–644.

[53] D. Yang, Choice of clear-sky model in solar forecasting, Journal of Renewable and Sustainable Energy 12 (2) (2020) 026101.

[54] X. Glorot, Y. Bengio, Understanding the difficulty of training deep feedforward neural networks, in: Proceedings of the thirteenth international conference on artificial intelligence and statistics, JMLR Workshop and Conference Proceedings, 2010, pp. 249–256.

[55] M. Lefèvre, A. Oumbe, P. Blanc, B. Espinar, B. Gschwind, Z. Qu, L. Wald, M. Schroedter-Homscheidt, C. Hoyer-Klick, A. Arola, et al., McClear: a new model estimating downwelling solar radiation at ground level in clear-sky conditions, Atmospheric Measurement Techniques 6 (9) (2013) 2403–2418.

[56] C. A. Gueymard, REST2: High-performance solar radiation model for cloudless-sky irradiance, illuminance, and photosynthetically active radiation–validation with a benchmark dataset, Solar Energy 82 (3) (2008) 272–285.

[57] R. Tapakis, A. G. Charalambides, Enhanced values of global irradiance due to the presence of clouds in Eastern Mediterranean, Renewable energy 62 (2014) 459–467.